

On the global oxygen anomaly and air-sea flux

Hernan E. Garcia¹ and Ralph F. Keeling

Scripps Institution of Oceanography, University of California, San Diego, La Jolla, California, USA

Abstract. We present a new climatology of monthly air-sea oxygen fluxes throughout the ice-free surface global ocean. The climatology is based on weighted linear least squares regressions using heat flux monthly anomalies for spatial and temporal interpolation of historical O₂ data. The seasonal oceanic variations show that the tropical belt (20°S–20°N) is characterized by relatively small air-sea fluxes when compared to the middle to high latitudes (40°–70°). The largest and lowest seasonal fluxes occur during summer and winter in both hemispheres. By means of an atmospheric transport model we show that our climatology is in better agreement with the observed amplitude and phasing of the variations in atmospheric O₂/N₂ ratios because of seasonal air-sea exchanges at baseline stations in the Pacific Ocean than with previous air-sea O₂ climatologies. Our study indicates that the component of the air-sea O₂ flux that correlates with heat flux dominates the large-scale air-sea O₂ exchange on seasonal timescales. The contribution of each major oceanic basin to the atmospheric observations is described. The seasonal net thermal (SNO_T) and biological (SNO_B) outgassing components of the flux are examined in relation to latitudinal bands, basin-wide, and hemispheric contributions. The Southern Hemisphere's SNO_B (~0.26 Pmol) and SNO_T (~0.29 Pmol) values are larger than the Northern Hemisphere's SNO_B (~0.15 Pmol) and SNO_T (~0.16 Pmol) values (1 Pmol = 10¹⁵ mol). We estimate a global extratropical carbon new production during the outgassing season of 3.7 Pg C (1 Pg = 10¹⁵ g), lower than previous estimates with air-sea O₂ climatologies.

1. Introduction

The oceanic O₂ flux contribution to the atmospheric O₂/N₂ ratio is primarily through seasonal-scale variability caused by a range of biochemical and physical processes across the air-sea interface. Biochemical processes include sources and sinks of O₂ due to marine production, respiration, and remineralization of organic matter. Physical processes include sources and sinks caused by water mass renewal or ventilation, air-sea gas exchange, solubility changes driven by seawater warming and cooling, near-surface turbulence and mixing whether induced by wind, waves, or small-scale breaking (i.e., bubble injection and spray), and aeolian inputs of labile substances. The seasonal distribution of surface O₂ anomalies and air-sea fluxes are useful to study the interplay between biochemical and physical processes that affect the O₂ concentration in seawater and its ultimate effect on the atmosphere. Two important aspects of studying the oceanic annual cycle of O₂ are to delimit sources and sinks of photosynthetic carbon production and air-sea exchange of CO₂ [e.g., Keeling *et al.*, 1993].

Najjar and Keeling [1997] estimated the mean annual cycle of dissolved O₂ anomalies ($\Delta[\text{O}_2]$) on the basis of spatial and temporal interpolation of National Oceanographic Data Center (NODC) historical data collected between 1900 and 1994. They binned the O₂ data in space and time increments. This causes difficulties in regions with poor monthly coverage. In areas of low temporal data coverage they used a 3 month or a 5 month time running average binning scheme to fill in missing values. Keeling *et al.* [1998] used the O₂ anomaly values from Najjar and Keeling [1997], the wind speeds of Wright [1988], and

different formulations of the gas exchange velocity to compute O₂ fluxes after correcting the O₂ anomaly data for sea level atmospheric pressure and sea surface skin temperature effects. Keeling *et al.* [1998] indicated that the fluxes derived from the Najjar and Keeling [1997] data underestimate the observed seasonal amplitude of the atmospheric O₂/N₂ ratios at baseline stations in the South Pacific Ocean by as much as 30%. They indicated that this underestimation resulted from seasonal smoothing in data sparse regions.

Najjar and Keeling [2000] presented a global climatology of monthly air-sea O₂ fluxes based on rescaling the O₂ anomaly values of Najjar and Keeling [1997] using the sea surface temperature (SST) climatology of Shea *et al.* [1992] and adding a correction for O₂ anomalies caused by air bubble injection. Keeling *et al.* [1998] described the SST rescaled climatology. Briefly, Keeling *et al.* [1998] averaged the SST climatology of Shea *et al.* [1992] into 12° latitudinal bands for each major ocean basin and calculated the fundamental harmonic amplitude of the averaged SST data. They then computed averaged SST values where concurrent O₂ anomaly values were available and computed the fundamental harmonic amplitude for this “reduced” SST data set in each 12° latitudinal band. They then calculated a scaling factor between the fundamental harmonic amplitudes of the averaged SST climatology and the reduced SST data. They multiplied the O₂ anomaly values of the Najjar and Keeling [1997] climatology by the scaling factor after subtracting the annual mean O₂ anomaly at each grid point. The SST-rescaled O₂ anomaly climatology was obtained after adding back the annual mean to each monthly value in the original O₂ anomaly value climatology. The SST-rescaled climatology improved the difference between the model-simulated and observed variations in the atmosphere when compared to the climatology without rescaling. However, the rescaled climatology still underestimated the amplitude of the atmospheric variations by about 20% at baseline stations located poleward of 30° latitude in the Northern and Southern Hemispheres.

Here we revisit the task of computing a representative global air-sea O₂ flux monthly climatology. The new climatology

¹Now at NOAA/NODC Ocean Climate Laboratory, Silver Spring, Maryland.

reduces excessive smoothing in O₂ data sparse regions. We outline an alternative method to that of *Najjar and Keeling* [1997, 2000] and *Keeling et al.* [1998] for estimating a global monthly climatology of sea surface O₂ anomaly and air-sea flux using selected historical O₂ data at observed depth levels. Our approach is based on binning the O₂ data by coarse spatial increments in latitude, and instead of binning the data by time of collection, we bin the O₂ data by fine increments in air-sea seasonal heat flux anomalies ($[\Delta Q]_{\text{sea}}$) independent of the time of year. Ocean heat flux is an objective, conservative variable. We use the $[\Delta Q]_{\text{sea}}$ data as a spatial and temporal template for interpolation of O₂ anomaly and flux values throughout the ice-free oceanic domain. Seasonal heat flux anomalies were chosen for interpolating the O₂ data because, as shown by *Keeling et al.* [1993], we expect a relationship between seasonal heat flux and air-sea O₂ flux regardless of whether the O₂ exchange is mediated by biological or physical processes. We compare our results to the *Keeling et al.* [1998] and the *Najjar and Keeling* [1997, 2000] data without air bubble injection correction. We find that the new flux climatology yields improved simulations of atmospheric O₂/N₂ variations.

Since the solubility of O₂ in seawater is primarily temperature-dependent, oceanic regions of net heating degas O₂ to the atmosphere, and oceanic regions of net cooling absorb atmospheric O₂. In this sense, air-sea O₂ flux is out of phase with temperature but in phase with heat flux. A similar relationship is expected for biologically mediated O₂ air-sea exchange whenever there is a strong correlation between primary production, oxygen production, and stratification. Increased vertical mixing during fall and winter driven by surface cooling brings nutrient-rich and carbon-rich, but relatively O₂-poor, water (less recently ventilated waters) to the mixed layer. Surface heat loss is thus associated with oceanic O₂ uptake. During spring and summer, vertical stratification reduces vertical mixing between surface (nutrient-poor, O₂-rich) and deeper (nutrient-rich, O₂-poor) waters. Biologically, O₂ production then increases because of increases in primary production that result from a combination of increased solar irradiance and available nutrients, and O₂ is released to the atmosphere. Surface heating is thus associated with biologically mediated O₂ outgassing. As the season progresses and vertical stratification occurs, nutrient concentrations and primary production generally decrease. The seasonal trends of surface heating and cooling and biological O₂ production suggest a correlation between heat flux anomalies and air-sea oxygen flux.

2. Data Sources and Data Quality

The primary data used in this study are discrete water samples with measured O₂ concentrations, in situ temperature (T , °C), and salinity (S) from selected near-sea surface historical oceanographic data. The hydrographic data are from the World Ocean Circulation Experiment, NODC archived data as of 1998, and the data compilations of *Reid* [1989, 1994], *Garcia* [1996], and *Garcia et al.* [1998]. The NODC data correspond to the world ocean database 1998. Typically, the bottle data consist of 12 or 24 depth discrete observations between the surface and the bottom. The O₂ data in volumetric units were converted to mass units ($\mu\text{mol kg}^{-1}$) using the molar volume of O₂ as a real gas and a density (ρ , kg m^{-3}) corresponding to T and S [*Millero and Poisson*, 1981]. The historical bottle data (918,489 observations) provide good coverage in the Northern Hemisphere and some parts of the Southern Hemisphere. We recognize that there is variability (i.e., diurnal, interannual, or longer timescale) inherent in the historical data, but this potential temporal bias is not treated here. In this study we take O₂ measured data in the upper 15 m of the water column to represent the distribution of O₂ in the surface layer.

The historical hydrographic data were collected over several years on different cruises. The precision of historical T , S , and pressure data are estimated to be $\pm 0.01^\circ\text{C}$, ± 0.01 , and ± 5 dbar, respectively [*Saunders*, 1986; *Garcia*, 1996]. We carried out a data quality control on the historical O₂ on several steps. We first rejected all measured O₂ data collected prior to 1960 because we believe that about this time more precise O₂ data began to be routinely collected. The hydrographic data were then sorted into 10° latitude by 10° longitude areas. We calculated the spatially averaged value for T , S , and O₂ and the standard error using all the data. Then, for each area we rejected spurious observations by means of variance and range checks on the historical data contained within these areas using O₂ against T and S plots. About 10% of the historical O₂ data were excluded by this data quality step. The precision of the historical O₂ data retained in this study is about $\pm 3 \mu\text{mol kg}^{-1}$.

3. Computation of O₂ Anomalies and Air-Sea Fluxes

The initial data processing step is the calculation of oxygen anomalies ($\Delta[\text{O}_2]$, $\mu\text{mol kg}^{-1}$) at every location where there were historical O₂, T , and S data. $\Delta[\text{O}_2]$ was evaluated as the difference between the measured O₂ concentration ($[\text{O}_2]_{\text{obs}}$) and the O₂ solubility ($[\text{O}_2]^*$) in seawater, $\Delta[\text{O}_2] = [\text{O}_2] - [\text{O}_2]^* + \delta_{\text{skin}}$, where δ_{skin} is the skin temperature correction. The $[\text{O}_2]^*$ values were computed as a function of T and S from the bottle data and sea level atmospheric pressure (P_a , atm) using the O₂ solubility equations of *Garcia and Gordon* [1992], the atmospheric pressure equation of *Benson and Krause* [1984], and the monthly atmospheric pressure climatology of *Oberhuber* [1988]. The precision of the O₂ solubility values is about 0.1–0.2% [*Garcia and Gordon*, 1992]. We assume complete O₂ equilibration with the atmosphere. The average atmospheric pressure corrections relative to mean sea level atmospheric pressure (1013 mbar) are typically about $\pm 4 \mu\text{mol kg}^{-1}$. For δ_{skin} we used the equation of *Hasse* [1971] with a depth for the bulk in situ temperature data from the hydrographic data of 2.5 m and the European Centre for Medium-Range Weather Forecasting (ECMWF) heat flux monthly climatology [*Gibson et al.*, 1997]. The δ_{skin} corrections are typically about $\pm 1 \mu\text{mol kg}^{-1}$. The δ_{skin} and P_a corrections combined are $\pm 4 \mu\text{mol kg}^{-1}$. The combined corrections are small when compared to the magnitude of the seasonal variations in $\Delta[\text{O}_2]$. We do not treat bubble injection corrections. There are no adequate constraints on the net effect of bubble injection on the global ocean gas flux, and the net seasonal effect is likely small [*Schudlich and Emerson*, 1996; *Keeling et al.*, 1998].

We evaluate air-sea O₂ fluxes (f_{O_2} , $\text{mol m}^{-2} \text{month}^{-1}$) using $f_{\text{O}_2} = \rho k_{\text{O}_2} \Delta[\text{O}_2]$, where k_{O_2} is the gas transfer velocity for O₂ (k_{O_2} , m s^{-1}). To calculate k_{O_2} , we use the formulation of *Wanninkhof* [1992] for long-term winds ($k_{\text{O}_2} = 0.39u^2(Sc_{\text{O}_2}/660)^{-1/2}$, where u (m s^{-1}) is wind speed and Sc_{O_2} is the Schmidt number for O₂). For calculating the Schmidt number we use the relation $Sc_{\text{O}_2} = 1638 - 81.83T + 1.483T^2 - 0.008004T^3$ [*Keeling et al.*, 1998] using SST values from *Shea et al.* [1992]. For wind speeds we use ECMWF monthly values [*Gibson et al.*, 1997]. We use the k_{O_2} formulation of *Wanninkhof* [1992] because it appears to be applicable to large-scale studies [*Keeling et al.*, 1998; *Najjar and Keeling*, 2000]. We computed f_{O_2} values for all locations with retained historical O₂ data.

4. Regression Analysis

The objective of the weighted linear least squares regression model is to estimate f_{O_2} as a function of monthly heat flux anomalies in 10° latitudinal bands covering the ice-free global ocean surface (80°S – 80°N). For evaluating the statistical weights

Table 1. List of Weighted Linear Least Squares Regression Coefficients Between Air-Sea O₂ Flux (f_{O_2} , mol m⁻² month⁻¹) and Heat Flux Monthly Anomalies ($[\Delta Q]_{\text{sea}}$, W M⁻²) in 10° Latitudinal Bands Covering the Entire Ice-Free World Ocean^a

Latitudinal Band	Northern Hemisphere	Southern Hemisphere
70°–80°	$a_0 = 3.519 \times 10^{-1} \pm 2.233 \times 10^{-2}$ $a_1 = 7.237 \times 10^{-3} \pm 1.552 \times 10^{-4}$ $r^2 = 0.84$	$a_0 = -1.367 \pm 6.666 \times 10^{-2}$ $a_1 = 9.115 \times 10^{-3} \pm 8.967 \times 10^{-4}$ $r^2 = 0.83$
60°–70°	$a_0 = -5.397 \times 10^{-2} \pm 1.084 \times 10^{-2}$ $a_1 = 1.140 \times 10^{-2} \pm 7.976 \times 10^{-5}$ $r^2 = 0.75$	$a_0 = 2.659 \times 10^{-1} \pm 2.606 \times 10^{-2}$ $a_1 = 5.944 \times 10^{-3} \pm 2.740 \times 10^{-4}$ $r^2 = 0.78$
50°–60°	$a_0 = 4.884 \times 10^{-1} \pm 7.060 \times 10^{-3}$ $a_1 = 1.118 \times 10^{-2} \pm 5.280 \times 10^{-5}$ $r^2 = 0.86$	$a_0 = 3.579 \times 10^{-1} \pm 2.237 \times 10^{-2}$ $a_1 = 1.176 \times 10^{-2} \pm 2.536 \times 10^{-4}$ $r^2 = 0.93$
40°–50°	$a_0 = -6.696 \times 10^{-1} \pm 1.045 \times 10^{-2}$ $a_1 = 1.085 \times 10^{-2} \pm 8.649 \times 10^{-5}$ $r^2 = 0.83$	$a_0 = 5.782 \times 10^{-1} \pm 2.577 \times 10^{-2}$ $a_1 = 1.240 \times 10^{-2} \pm 2.448 \times 10^{-4}$ $r^2 = 0.92$
30°–40°	$a_0 = -1.883 \times 10^{-1} \pm 6.120 \times 10^{-3}$ $a_1 = 5.936 \times 10^{-3} \pm 4.029 \times 10^{-5}$ $r^2 = 0.83$	$a_0 = 7.104 \times 10^{-1} \pm 1.483 \times 10^{-2}$ $a_1 = 4.170 \times 10^{-3} \pm 1.528 \times 10^{-4}$ $r^2 = 0.57$
20°–30°	$a_0 = -1.451 \times 10^{-1} \pm 6.501 \times 10^{-3}$ $a_1 = 5.078 \times 10^{-3} \pm 5.663 \times 10^{-5}$ $r^2 = 0.98$	$a_0 = 6.088 \times 10^{-1} \pm 1.434 \times 10^{-2}$ $a_1 = 3.837 \times 10^{-3} \pm 1.740 \times 10^{-4}$ $r^2 = 0.61$
10°–20°	$a_0 = -7.412 \times 10^{-2} \pm 1.157 \times 10^{-2}$ $a_1 = 7.252 \times 10^{-4} \pm 2.190 \times 10^{-4}$ $r^2 = 0.55$	$a_0 = -1.170 \times 10^{-2} \pm 1.565 \times 10^{-2}$ $a_1 = 3.898 \times 10^{-3} \pm 2.686 \times 10^{-4}$ $r^2 = 0.43$
0°–10°	$a_0 = 1.398 \times 10^{-1} \pm 6.336 \times 10^{-3}$ $a_1 = -8.492 \times 10^{-4} \pm 2.392 \times 10^{-4}$ $r^2 = 0.35$	$a_0 = 7.069 \times 10^{-4} \pm 1.037 \times 10^{-2}$ $a_1 = -1.719 \times 10^{-3} \pm 3.551 \times 10^{-4}$ $r^2 = 0.38$

^aThe regressions are of the form $f_{O_2} = (a_0 \pm \sigma_0) + (a_1 \pm \sigma_1)[\Delta Q]_{\text{sea}}$, where a_0 and a_1 represent the intercept and slope of the regressions and σ_0 and σ_1 represent the standard error of the a_0 and a_1 coefficients. The regression uses as weights the standard error of the f_{O_2} data binned in $[\Delta Q]_{\text{sea}}$ increments of 50 W m⁻². The r^2 values represent the determination coefficients of the regressions.

for the f_{O_2} data in each 10° latitudinal band both the f_{O_2} and the monthly heat flux anomaly values were processed through a three-step data processing scheme. First, we computed monthly heat flux anomalies ($[\Delta Q]_{\text{sea}}$, W m⁻²) at each point of the ECMWF grid by subtracting the annual mean heat flux value from each monthly value. Second, a monthly $[\Delta Q]_{\text{sea}}$ value corresponding to the geographical location and month of collection of every f_{O_2} data value was calculated as follows. The $[\Delta Q]_{\text{sea}}$ value corresponding to each of the f_{O_2} data value was found by first locating the monthly heat flux anomaly value in the ECMWF climatology equal to the month of each O₂ observation and then using spatial interpolation between adjacent $[\Delta Q]_{\text{sea}}$ grid points to assign a $[\Delta Q]_{\text{sea}}$ value to each f_{O_2} data value according to its geographical position. Third, we divided the f_{O_2} data set into 10° latitudinal bands between 80°N and 80°S without overlapping and binned the f_{O_2} values within monthly $[\Delta Q]_{\text{sea}}$ increments of 50 W m⁻² in each 10° latitudinal band. The choice of 50 W m⁻² increments in $[\Delta Q]_{\text{sea}}$ is a qualitative compromise between having a relatively large number of f_{O_2} data points and low resolution in $[\Delta Q]_{\text{sea}}$ and having a high resolution in $[\Delta Q]_{\text{sea}}$ with a small number of f_{O_2} data values in any particular latitudinal band. We then computed the mean and standard errors of the f_{O_2} values regardless of month of collection and geographic location within each $[\Delta Q]_{\text{sea}}$ increment. We use the midpoint value of the 50 W m⁻² $[\Delta Q]_{\text{sea}}$ increments to bin the f_{O_2} values. Values of f_{O_2} that differed by more than 4 standard deviations from their mean values in each $[\Delta Q]_{\text{sea}}$ increment were rejected from further analysis. This data quality control step eliminated about 5% of the O₂ data. We then evaluated the mean and standard errors for the retained f_{O_2} values at every 50 W m⁻² $[\Delta Q]_{\text{sea}}$ increment within each 10° latitudinal band. Thus all bins with data were evaluated independently according to the statistical information in each bin. The data processing described above yields the mean and standard errors of f_{O_2} values binned in each $[\Delta Q]_{\text{sea}}$ increment for all the data geographically located in each 10° latitudinal band.

We performed weighted linear least squares regressions between $[\Delta Q]_{\text{sea}}$ as the independent variable and f_{O_2} as the dependent variable for all the data in 10° latitudinal bands of the general form $f_{O_2} = a_0 + a_1[\Delta Q]_{\text{sea}}$, where a_0 and a_1 are the intercept and slope regression coefficients. We assume that the variance in the regressions is due solely to the f_{O_2} data. Thus, in calculating the regression coefficients for each 10° latitudinal band we used weights based on the standard error of the f_{O_2} data binned in each $[\Delta Q]_{\text{sea}}$ increment. The purpose of the weights in the calculation of the regression coefficients is to provide more importance to f_{O_2} values whose variance factors are smaller and less importance to f_{O_2} values whose variance factors are larger at every $[\Delta Q]_{\text{sea}}$ increment. Thus the regression coefficients are sensitive to the statistical information in the f_{O_2} values. Table 1 lists the $f_{O_2} = a_0 + a_1[\Delta Q]_{\text{sea}}$ regression coefficients.

Plate 1 shows the magnitude of the slope regression coefficients (a_1) for each 10° latitudinal band. The coefficients show large north-south gradients within the Northern and Southern Hemispheres and are generally asymmetrical about the equator. The a_1 coefficients increase poleward, reaching maximum values between 40° and 70°. The Southern Hemisphere shows higher a_1 values with a somewhat narrower latitudinal peak centered near 45°S than at comparable latitudes in the Northern Hemisphere. Poleward of 70° latitude, the a_1 values decrease because of increased seasonal sea-ice coverage and decreases in the wind gas exchange and wind speeds. Between 10°N and 10°S the coefficients are near zero or even slightly negative. The equatorial waters show large $\Delta[O_2]$ values that can be attributed to upwelling of waters highly undersaturated with respect to O₂. However, the surface waters exhibit relatively small seasonal changes in f_{O_2} and $[\Delta Q]_{\text{sea}}$ when compared to surface waters at middle to high latitudes. For statistical comparison the coefficient of determination (r^2) is >0.6 poleward of 20°, reaching maximum values (≥ 0.8) poleward of about 40° latitude. The r^2 values are >0.4 between 20°S and 20°N (Table 1).

We also carried out separate regression analysis between f_{O_2} and $[\Delta Q]_{\text{sea}}$ for data located in the Atlantic, Pacific, and Indian

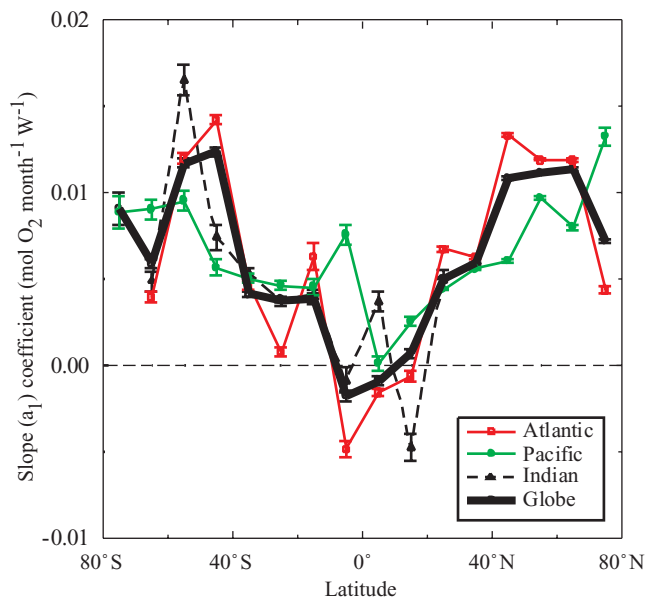


Plate 1. Values of the slope (a_1) coefficients from the weighted linear least squares regression between air-sea O₂ flux and seasonal heat flux anomalies ($f_{O_2} = a_0 + a_1[\Delta Q]_{\text{sea}}$) for the Atlantic, Pacific, and Indian basins and for the entire ocean domain. The vertical error bars represent the ± 1 standard deviation of the regression coefficients in each 10° latitudinal band.

Oceans in each 10° latitudinal band (Plate 1). The main reason for evaluating separate regression analysis in each major ocean basin is because differing sampling density between basins could bias the magnitude of the global regression coefficients toward values appropriate for the basins with the largest number of observations. We adopt subjective definitions for the geographical boundaries of the major ocean basins. The latitudinal patterns of the a_1 coefficients in each basin show similar features as the global a_1 coefficients, although some differences are notable (Plate 1). The North Atlantic shows the largest a_1 values except north of 70°N and south of 50°S. The Indian Ocean slope coefficients show the largest positive values centered near 50°S.

What is the effect of k_{O_2} on the computed air-sea O₂ fluxes as a function of latitude? To examine the effect of k_{O_2} alone, we carried out a weighted regression analysis between $\Delta[O_2]$ and $[\Delta Q]_{\text{sea}}$ of the form $\Delta[O_2] = b_0 + b_1[\Delta Q]_{\text{sea}}$, where b_0 and b_1 are the intercept and slope regression coefficients. We followed the same procedure described earlier for obtaining the a_0 and a_1 coefficients in each 10° latitudinal band. Any latitudinal differences between b_1 ($\Delta[O_2]/[\Delta Q]_{\text{sea}}$) and a_1 ($f_{O_2}/[\Delta Q]_{\text{sea}}$) reflect the effect of k_{O_2} differences because this is the only free parameter. Plate 2 shows the latitudinal variation of the b_1 slope coefficients. The b_1 coefficients increase poleward nearly monotonically (Plate 2), while the a_1 coefficients increase poleward, reaching maximum values between 40° and 70° and decrease poleward of 70° latitude as described earlier (Plate 1). Thus the decrease in the a_1 values observed at high and low latitudes reflects latitudinal decreases in wind speed values. Table 2 lists the $\Delta[O_2] = b_0 + b_1[\Delta Q]_{\text{sea}}$ regression coefficients.

The latitudinal distribution of the regression coefficients is subject to uncertainty resulting from sampling errors, data variability, the effect of differing sampling density between latitudinal bands and between basins, and covariance effects between f_{O_2} , k_{O_2} , and $[\Delta Q]_{\text{sea}}$. It is difficult to quantify these effects. We believe that the a_1 regression coefficients are representative of the mean large-scale air-sea O₂ flux variability on seasonal timescales across each

10° latitudinal band, and we demonstrate this later. First, the regression coefficients obtained for the Atlantic, Pacific, and Indian Oceans closely follow the latitudinal trends of the global regression coefficients (Plates 1 and 2). Second, evaluating linear regressions over 5° latitudinal bands did not yield significantly different regression coefficients than those obtained using 10° bands. Third, the latitudinal distribution of the a_1 coefficients indicates real north-south trends. Fourth, as shown below, the correlation between f_{O_2} and $[\Delta Q]_{\text{sea}}$ as a function of latitude captures most of the variation in O₂/N₂ as seen in the atmosphere. The sensitivity of the regressions coefficients to covariance between f_{O_2} , k_{O_2} , and $[\Delta Q]_{\text{sea}}$ is difficult to quantify. We believe that the most important source of error in the calculation of f_{O_2} values is the variability in the O₂ data.

5. Global Distribution of Seasonal Air-Sea O₂ Fluxes

To obtain a global distribution of monthly f_{O_2} values, we use the regression coefficients (a_0 and a_1) as linear-scale functions of $[\Delta Q]_{\text{sea}}$. We calculated f_{O_2} values at every grid point of the $[\Delta Q]_{\text{sea}}$ climatology both spatially and temporally within the 10° latitudinal bands. We used a linear interpolation scheme to obtain f_{O_2} values between the midpoint of the 10° latitudinal bands. We calculated seasonal anomalies in air-sea fluxes (f_{O_2})_{sea} at every grid point according to $(f_{O_2})_{\text{sea}} = a_1[\Delta Q]_{\text{sea}}$. The annual mean of $(f_{O_2})_{\text{sea}}$ computed this way is zero because $[\Delta Q]_{\text{sea}}$ also has zero annual mean. The mean annual f_{O_2} does not contribute measurably to seasonal variation in the atmospheric O₂/N₂ ratio [Keeling *et al.*, 1998]. Only the seasonal component of the air-sea O₂ flux is needed in our atmospheric simulation as shown below. We set the $(f_{O_2})_{\text{sea}}$ values to zero poleward of 80° latitude and in ice-covered regions using the SST data of Shea *et al.* [1992].

Maps of the distribution of the monthly anomalies of air-sea O₂ fluxes show strong meridional gradients reflecting the

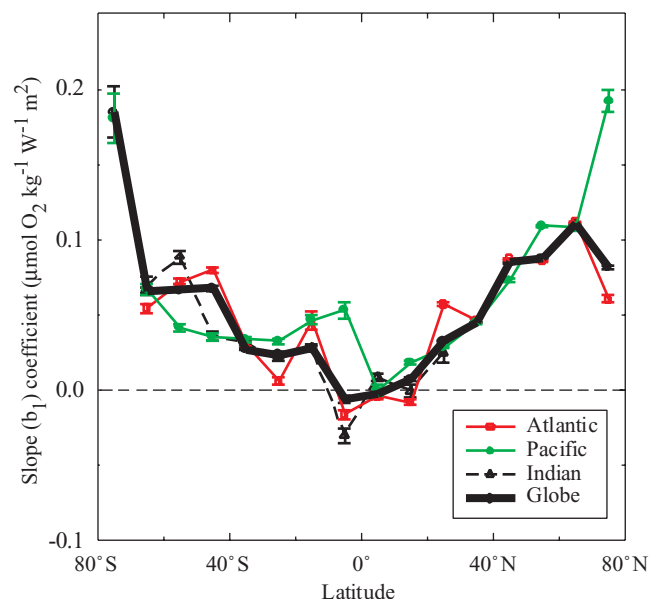


Plate 2. Values of the slope (b_1) coefficients from the weighted linear least squares regression between O₂ anomaly and seasonal heat flux anomalies ($\Delta[O_2] = b_0 + b_1[\Delta Q]_{\text{sea}}$) for the Atlantic, Pacific, and Indian basins and the entire ocean domain. The vertical error bars represent the ± 1 standard deviation of the regression coefficients in each 10° latitudinal band.

Table 2. Weighted Linear Least Squares Regression Coefficients Between Air-Sea O₂ Anomalies ($\Delta[\text{O}_2]$, $\mu\text{mol kg}^{-1}$) and Heat Flux Monthly Anomalies ($[\Delta Q]_{\text{sea}}$, W m^{-2}) in 10° Latitudinal Bands Covering the Entire Ice-Free World Ocean^a

Latitudinal Band	Northern Hemisphere	Southern Hemisphere
70°–80°	$b_0 = 5.707 \pm 2.073 \times 10^{-1}$ $b_1 = 8.158 \times 10^{-2} \pm 1.495 \times 10^{-3}$ $r^2 = 0.81$	$b_0 = -2.412 \times 10^1 \pm 1.142$ $b_1 = 1.848 \times 10^{-1} \pm 1.660 \times 10^{-2}$ $r^2 = 0.94$
60°–70°	$b_0 = 2.622 \pm 7.691 \times 10^{-2}$ $b_1 = 1.107 \times 10^{-1} \pm 6.093 \times 10^{-4}$ $r^2 = 0.84$	$b_0 = 2.143 \pm 1.882 \times 10^{-1}$ $b_1 = 6.542 \times 10^{-2} \pm 2.199 \times 10^{-3}$ $r^2 = 0.88$
50°–60°	$b_0 = 6.514 \times 10^{-1} \pm 4.203 \times 10^{-2}$ $b_1 = 8.785 \times 10^{-2} \pm 3.242 \times 10^{-4}$ $r^2 = 0.80$	$b_0 = 2.078 \pm 1.173 \times 10^{-1}$ $b_1 = 6.665 \times 10^{-2} \pm 1.354 \times 10^{-3}$ $r^2 = 0.95$
40°–50°	$b_0 = -3.596 \pm 6.764 \times 10^{-2}$ $b_1 = 8.497 \times 10^{-2} \pm 5.888 \times 10^{-4}$ $r^2 = 0.77$	$b_0 = 2.972 \pm 1.375 \times 10^{-1}$ $b_1 = 6.764 \times 10^{-2} \pm 1.324 \times 10^{-3}$ $r^2 = 0.91$
30°–40°	$b_0 = -2.553 \times 10^{-1} \pm 4.070 \times 10^{-2}$ $b_1 = 4.518 \times 10^{-2} \pm 2.728 \times 10^{-4}$ $r^2 = 0.92$	$b_0 = 4.786 \pm 1.036 \times 10^{-1}$ $b_1 = 2.747 \times 10^{-2} \pm 1.034 \times 10^{-3}$ $r^2 = 0.54$
20°–30°	$b_0 = -5.939 \times 10^{-1} \pm 4.396 \times 10^{-2}$ $b_1 = 3.295 \times 10^{-2} \pm 3.590 \times 10^{-4}$ $r^2 = 0.93$	$b_0 = 4.409 \pm 1.103 \times 10^{-1}$ $b_1 = 2.377 \times 10^{-2} \pm 1.288 \times 10^{-3}$ $r^2 = 0.48$
10°–20°	$b_0 = -7.307 \times 10^{-1} \pm 6.982 \times 10^{-2}$ $b_1 = 7.370 \times 10^{-3} \pm 1.252 \times 10^{-3}$ $r^2 = 0.38$	$b_0 = -4.779 \times 10^{-1} \pm 1.220 \times 10^{-1}$ $b_1 = 2.758 \times 10^{-2} \pm 1.704 \times 10^{-3}$ $r^2 = 0.43$
0°–10°	$b_0 = 1.375 \pm 5.356 \times 10^{-2}$ $b_1 = -2.566 \times 10^{-3} \pm 1.971 \times 10^{-3}$ $r^2 = 0.41$	$b_0 = -1.281 \pm 9.573 \times 10^{-2}$ $b_1 = -5.868 \times 10^{-3} \pm 2.821 \times 10^{-3}$ $r^2 = 0.27$

^aThe regressions are of the form $\Delta[\text{O}_2] = (b_0 \pm \sigma_0) + (b_1 \pm \sigma_1)[\Delta Q]_{\text{sea}}$, where b_0 and b_1 represent the intercept and slope of the regressions and σ_0 and σ_1 are the standard error of the b_0 and b_1 coefficients. The regression uses as weights the standard error of the ($\Delta[\text{O}_2]$) data binned in $[\Delta Q]_{\text{sea}}$ increments of 50 W m^{-2} . The r^2 values represent the determination coefficients of the regressions.

seasonal variation of the distribution of winds (exchange velocity), seasonal heat fluxes, and biological production. For brevity we show maps for December and June, the months with the largest seasonal fluxes (Plate 3). The seasonal pattern of O₂ flux anomalies in both hemispheres is characterized by sea-to-air fluxes during summer and air-to-sea fluxes during winter. This hemispheric pattern is consistent with warming, vertical stratification, and high rates of primary production during summer and cooling, enhanced vertical mixing, and low rates of primary production during winter throughout most of the open surface ocean. In the Northern Hemisphere, fluxes generally increase poleward to about 60°N and decrease north of this latitude. In contrast, in the Southern Hemisphere the fluxes are largest over a relatively narrow latitudinal belt centered near 50°S.

6. Simulated and Observed O₂/N₂ Ratios in the Atmosphere

We use our estimated $[f_{\text{O}_2}]_{\text{sea}}$ values to simulate the seasonal variability in the air O₂/N₂ ratio by means of the TM2 atmospheric transport model [Heiman, 1995]. Briefly, the TM2 model is a three-dimensional advection model with a spatial resolution of about $7.5^\circ \times 7.5^\circ$ and nine vertical levels. We initialize the atmospheric transport model using the $[f_{\text{O}_2}]_{\text{sea}}$ values and the ECMWF wind climatology for the year 1986. Steady state results are typically reached after the fourth year after initialization of the TM2 model. The model results are then compared to interannually detrended O₂/N₂ observations collected at time series stations located mainly in the Pacific (Table 3). The oceanic component of the detrended data is isolated, correcting the data for land photosynthesis and respiration using CO₂ data following Keeling *et al.* [1998]. To predict changes in the oceanic O₂/N₂ ratio, it is necessary also to account for the small seasonal N₂ variation in the atmosphere due to air-sea N₂ exchange (f_{N_2}). The f_{N_2} values were computed as the product of ECMWF seasonal heat flux anomaly times the temper-

ature derivative of the N₂ solubility ($[\text{N}_2]^*$). The $[\text{N}_2]^*$ values were computed using the solubility equation of Weiss [1970] as a function of SST [Shea *et al.*, 1992]. We subtracted the annual mean value from the monthly N₂ flux to get the seasonal component $[f_{\text{N}_2}]_{\text{sea}}$. The seasonal cycles for the simulated and observed O₂/N₂ cycles are fitted using a four-harmonic seasonal cycle. We adopt the “per meg” unit to compare the oceanic and atmospheric O₂/N₂ variations [Keeling *et al.*, 1993].

We do not simulate separately the contribution of the annual mean O₂ and N₂ fluxes to the atmospheric O₂/N₂ changes. Our interest here is the seasonal cycles in O₂/N₂ for which the annual mean fluxes appear to be insignificant as shown by Keeling *et al.* [1998]. Plate 4a shows a comparison between the model-simulated and the measured O₂/N₂ cycles. The agreement between the simulated and observed O₂/N₂ variations is very good, particularly at the middle- to high-latitude time series stations where the largest seasonal variations are found. The timing of the air cycle in both hemispheres generally follows the timing of the cycle of oceanic ingassing in winter and outgassing in summer. The simulated O₂/N₂ variations based on the global regression coefficients lead the atmospheric observations by slightly less than a month. Except for La Jolla the simulated values of the peak-to-peak amplitude are within 10% of the observed amplitude. At La Jolla the simulated amplitude is too low by about a factor of 0.6. The Kumukahi station has the largest phase difference, about a month. Even neglecting the biological component, some phase lag is expected on the basis of mixed layer equilibration time for O₂ of a few weeks that our model simulations neglect. Also, a phase lag in the biological component is expected because of the lagged response of photosynthesis to seasonal stratification and nutrient availability.

The contribution of the major ocean basins to the observed O₂/N₂ variation is shown in Plate 4b. The amplitude and phasing of the seasonal oceanic cycles at the baseline stations is dominated by the O₂/N₂ contributions from the Pacific and Atlantic basins. The contribution of the Indian Ocean to the Pacific O₂/N₂ ratio plays a smaller but not insignificant role. The results suggest that the large-

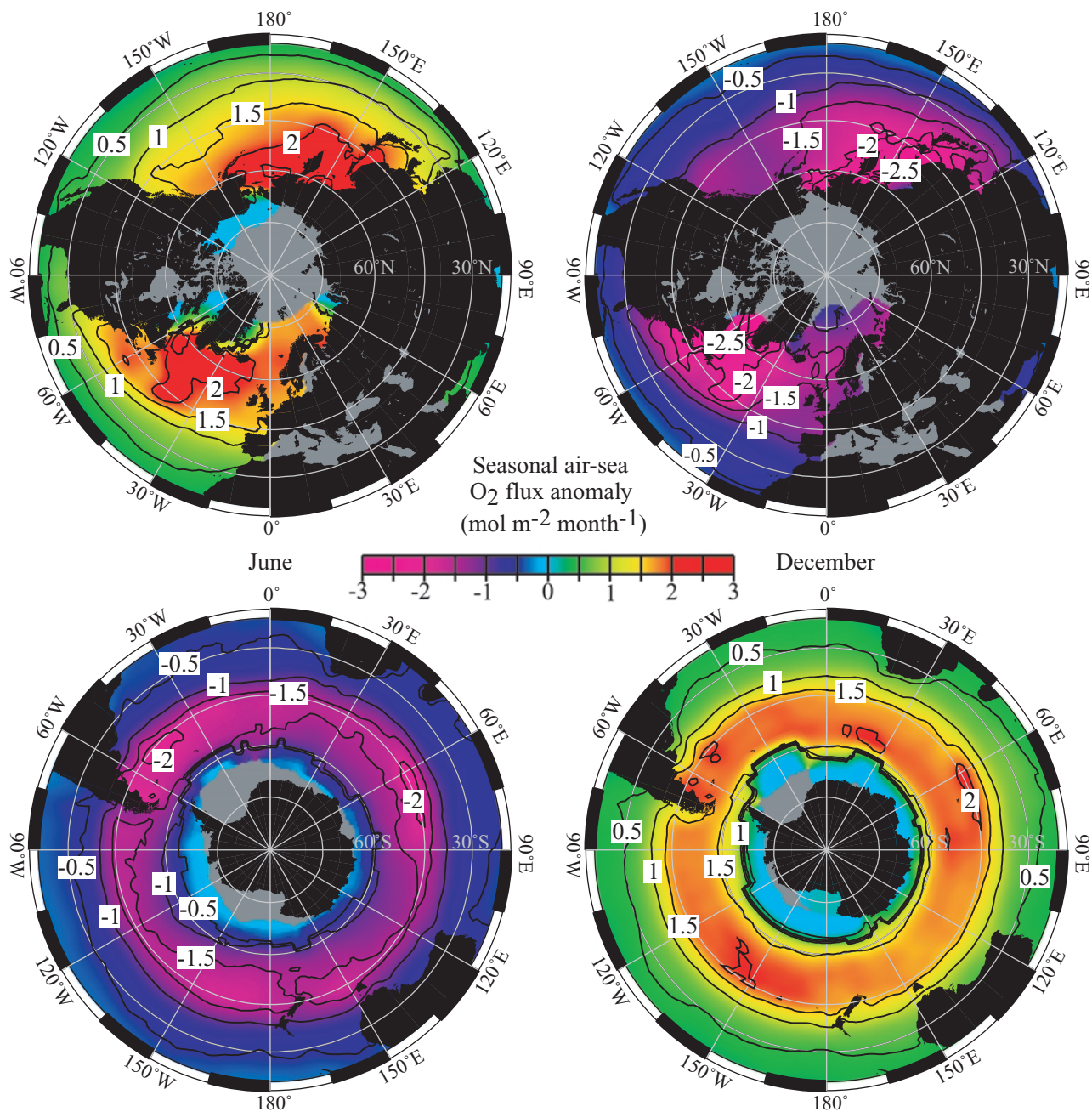


Plate 3. Distribution of the anomaly in seasonal air-sea oxygen fluxes in the (top) Northern and (bottom) Southern Hemispheres poleward of 20° latitude during (left) June and (right) December. Positive fluxes indicate sea-to-air fluxes, while negative fluxes represent air-to-sea fluxes. The largest fluxes are observed between 30° and 60° latitude in both hemispheres. Fluxes poleward of 80° latitude are set to zero.

scale contribution of each basin to the O₂/N₂ variations is most sensitive to the north-south distribution of O₂ surface fluxes and, to a lesser extent, to zonal distribution because the atmosphere smoothes out east-west trends.

Simulations based on the O₂ anomaly climatology of *Najjar and Keeling* [1997] are shown for comparison purposes in Plate 4c. Results are shown using the *Najjar and Keeling* [1997] climatology both with and without SST rescaling. The

Table 3. Sampling Stations in the Scripps O₂/N₂ Network^a

Station Code	Location	Position	Elevation, m	Time Period
ALT	Alert, Northwest Territories	82°27'N 62°31'W	210	April 1991 to May 1996
CBA	Cold Bay, Alaska	55°12'N 162°43'W	25	Aug. 1995 to July 1996
NWR	Niwot Ridge, Colorado	40° 3'N 105°38'W	3749	April 1991 to Jan. 1993
LJO	La Jolla, California	32°52'N 117°15'W	20	May 1989 to June 1996
KUM	Kumukahi, Hawaii	19°31'N 154°49'W	40	June 1993 to July 1996
MLO	Mauna Loa, Hawaii	19°32'N 155°35'W	3397	Aug. 1993 to July 1996
SMO	Cape Matatula, U.S. Samoa	14°15'S 170°34'W	42	June 1993 to July 1996
CGO	Cape Grim, Tasmania	40°41'S 144°41'E	94	Jan. 1991 to July 1996
SPO	South Pole	89°59'S 24°48'W	2810	Nov. 1991 to Feb. 1996

^a After Keeling *et al.* [1998].

model simulations based on the *Najjar and Keeling* [1997] climatology underestimate the observed O₂/N₂ cycles poleward of 31° latitude on average by about 15% in the Northern Hemisphere and by 23% in the Southern Hemisphere. A particularly large discrepancy is seen at Samoa (SMO) station (14°S), a result not explained by Keeling *et al.* [1998]. Model simulations based on our climatology are generally in better agreement with observations, particularly at Samoa, suggesting that the *Najjar and Keeling* [1997] climatology may be inaccurate in the tropical South Pacific. On the other hand, the lack of atmospheric observations at additional baseline locations in the tropical Pacific makes it difficult to draw firm conclusions, and the discrepancy could be caused by other errors such as uncertain atmospheric transports, in which case our model simulations are in agreement fortuitously.

7. Sensitivity Analysis of the Simulated O₂/N₂ Variations

To assess the significance of the hemispheric $[f_{O_2}]_{sea}$ values, we compared the effect of the $(f_{O_2})_{sea}$ latitudinal gradients in each hemisphere on the observed O₂/N₂ ratio in the atmosphere by means of the TM2 model. We calculated $[f_{O_2}]_{sea}$ values in the Southern Hemisphere using the a_1 regression coefficients for the Northern Hemisphere. We calculated also $[f_{O_2}]_{sea}$ values in the Northern Hemisphere using the a_1 regression coefficients for the Southern Hemisphere. We then initialized the TM2 model with the new set of $[f_{O_2}]_{sea}$ values. The results of the simulations indicate that the amplitudes of the atmospheric cycles at the baseline stations are too low or too high by as much as 40% depending on the baseline station. This suggests that the magnitude and latitudinal gradient of the a_1 coefficients shown in Plate 1 are significant and reflect real features in amplitude and phasing of the cycles in each hemisphere. The results also indicate that there is little interhemispheric mixing on seasonal timescales with respect to O₂.

We also assessed the sensitivity of the simulated O₂/N₂ variations to the choice of global and basin-wide regression coefficients. We initialized the TM2 model using $[f_{O_2}]_{sea}$ that we obtained from the a_1 regression coefficients estimated independently in the Atlantic, Pacific, and Indian basins. Using these basin a_1 coefficients produced changes in the amplitude of the oceanic cycles at the baseline stations of about ±10% depending on location when compared to the fluxes obtained using the global a_1 coefficients. This means that the magnitude and latitudinal gradient of the global a_1 coefficients capture the essential large-scale features of the air-sea O₂ flux. We cannot discard the possibility that finer spatial and temporal resolution of the a_0 and a_1 values might improve the simulated O₂/N₂ cycles. In summary, the results indicate that the regression approach provides a representative prediction of the seasonal air-sea O₂ flux and the oceanic O₂/N₂ variations when compared to the atmospheric observations.

8. Wind Exchange Coefficient Calibration

One approach to achieve a better quantitative agreement between the simulated and observed atmospheric O₂/N₂ variations is to scale the global oceanic O₂ flux field by a constant, dimensionless correction or calibration factor while fixing the seasonal N₂ flux. This factor can be viewed as a multiplicative correction to the air-sea O₂ gas exchange coefficient. Keeling *et al.* [1998] optimized the gas exchange velocity for O₂ on the basis of the *Najjar and Keeling* [1997] climatology using the algorithm of *Heiman and Keeling* [1989]. The algorithm yields scaling factors that minimize the sum of squared residuals between the observed and simulated atmospheric O₂/N₂ cycles in the least squares sense. Here we used the same algorithm to estimate scaling factors for the O₂ exchange velocities on the basis of the present climatology. We refer to this scaling factor as atmospheric calibration.

Table 4 lists atmospheric calibrations based on the present O₂ flux climatology as well as correction factors computed previously by Keeling *et al.* [1998] using the *Najjar and Keeling* [1997] climatology. Except for the La Jolla station all of the atmospheric calibrations are very close to 1. We find that the atmospheric calibration for simultaneous fitting of all the stations is 1.01 ± 0.05 . The atmospheric calibrations for the high-latitude stations range between 1.09 ± 0.09 in the Northern Hemisphere (ALT, CBA, and NWR) and 0.97 ± 0.08 in the Southern Hemisphere (CGO and SPO). In contrast, Keeling *et al.* [1998] obtained larger atmospheric calibrations for the same grouping of stations: 1.14 ± 0.05 for all the stations, while for the high-latitude stations the scaling factors ranged between 1.15 ± 0.05 (ALT, CBA, and NWR) and 1.23 ± 0.06 (CGO and SPO) as shown in Table 4.

The results indicate that the regression approach provides a representative simulated atmospheric O₂/N₂ variation without the need for atmospheric calibration factors. The combined use of the surface O₂ anomaly data of this work and the k_{O_2} formulation of *Wanninkhof* [1992] yield simulated O₂/N₂ variations in good agreement with the atmospheric O₂/N₂ observations. The results substantiate the use of the *Wanninkhof* [1992] relation for computing air-sea gas exchange rates at large spatial and monthly timescales. For the remainder of the discussion we use the uncalibrated O₂ flux climatology, except where noted.

9. Biological and Thermal Components of the Air-Sea Flux

We represent f_{O_2} as the sum of thermal (f_T) and biological (f_B) fluxes. Following Keeling *et al.* [1993], we compute the f_T component using

$$f_T = -\frac{d[O_2]^*}{dT} \frac{Q}{c_p},$$

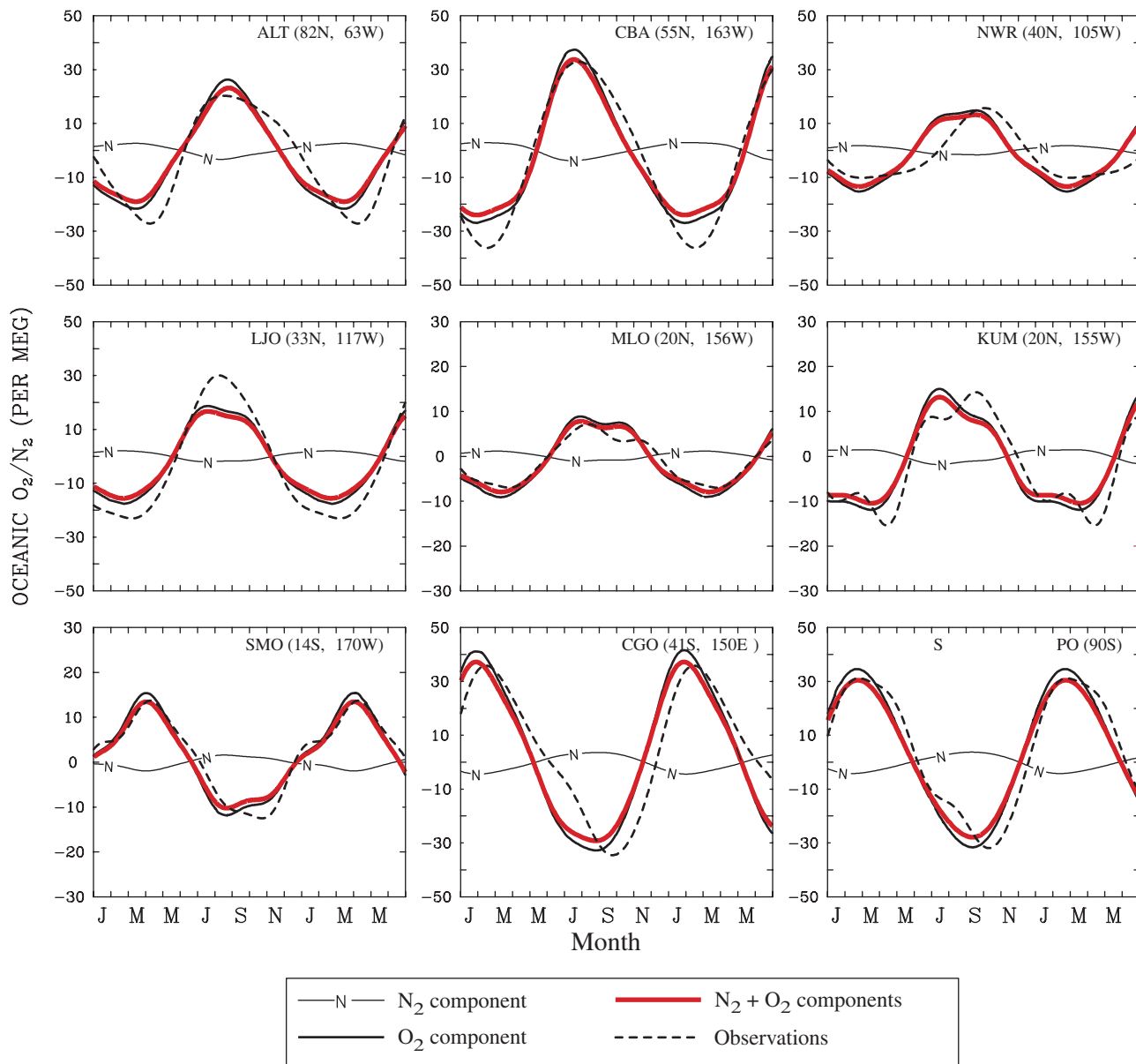


Plate 4a. Model-simulated (heavy black solid curve) and observed (black dashed curve) oceanic components of the atmospheric O₂/N₂ cycle at the Pacific Ocean baseline stations. The simulated O₂ component of the O₂/N₂ cycle is based on weighted linear least squares regression between air-sea O₂ flux and seasonal heat flux anomalies (see text for details). The dashed curve represents the observed oceanic component of the atmospheric O₂/N₂ cycle based on least squares fit to the observations using a terrestrial O₂:C ratio of 1.1. The black curve labeled N represents the N₂ flux variation based on net heat flux data.

where Q is heat flux, c_p is heat capacity of seawater ($3992 \text{ J kg}^{-1} \text{ }^\circ\text{C}^{-1}$), and T is temperature ($^\circ\text{C}$). We evaluate f_T at every grid point of the f_{O_2} climatology and calculate the seasonal thermal component $[f_T]_{\text{sea}}$ by subtracting the annual mean from each monthly value. We evaluate the seasonal biological component $[f_B]_{\text{sea}}$ as the difference between the total seasonal flux and the thermal component using $[f_B]_{\text{sea}} = [f_{O_2}]_{\text{sea}} - [f_T]_{\text{sea}}$. Because f_T assumes complete O₂ equilibration with the air, its seasonal amplitude might be overestimated, and $[f_B]_{\text{sea}}$ might be underestimated. Thus the biological component of the flux represents a conservative lower limit when there is no O₂ equilibration of surface waters with the atmosphere. As described earlier, we set all fluxes equal to zero in ice-covered waters.

10. Seasonal Net Outgassing

One index of the seasonal air-sea O₂ flux exchange is seasonal net outgassing (SNO) defined by *Keeling and Shertz* [1992] as the spatially and temporally integrated oxygen flux over the annual periods when the spatially integrated flux is positive (e.g., sea to air). *Najjar and Keeling* [2000] adopted a slightly different definition of SNO than *Keeling and Shertz* [1992] in which the annual mean O₂ flux is subtracted before integration. The difference in the definition is insignificant at the hemispheric scale, and the latter definition is perhaps more appropriate on smaller spatial scales as a measure of the contribution to seasonal variations in atmospheric O₂/N₂. Here we follow the *Najjar and Keeling* [2000] definition of SNO and compute also both the thermal (SNO_T) and

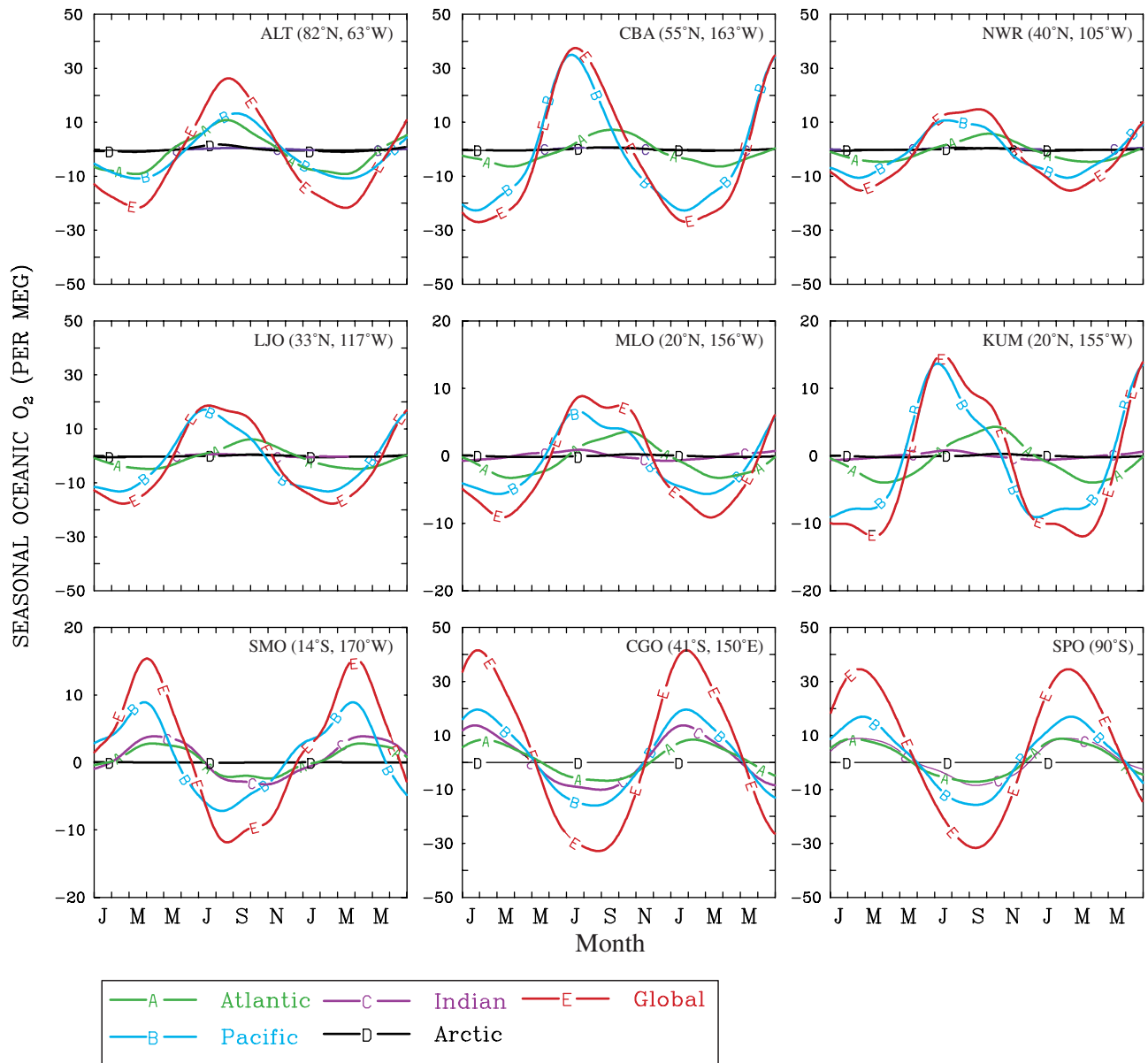


Plate 4b. Model-simulated contributions to the oceanic O₂ component for the Atlantic (green curve), Pacific (blue curve), Indian (purple curve), Arctic (black curve), and global ocean (red curve). The simulated component for individual basins is based on the global regressions coefficients (a_1) applied to 10° latitudinal bands in each basin.

biological (SNO_B) seasonal net outgassing. To compute SNO, we first subtracted the annual mean flux from each monthly flux value and then integrated over the months when the fluxes are positive. We carried out this calculation on hemispheric and latitudinal bands for the global ocean and major ocean basins. We computed SNO_T and SNO_B in a similar manner as SNO using the f_T and f_B monthly climatology. The calculation of SNO is sensitive to the area of integration as well as the phasing of the flux fields. For simplicity, SNO, SNO_T, and SNO_B values are reported in units of 10¹⁴ mol O₂.

Table 5 lists SNO_T and SNO_B values for selected latitudinal ranges in the global ocean and ocean basins. We computed the global SNO_B (4.2) and SNO_T (4.5) values by summing the thermal and biological hemispheric results (Table 5). The SNO_B:SNO_T ratio provides insight into the contribution of thermal and biological sources. The SNO_B:SNO_T ratio in the

Southern Hemisphere is 0.9, while the ratio in the Northern Hemisphere is 1.0. This suggests that the thermal and biological hemispheric averaged contributions to SNO are roughly equal. The extratropical (>30°) SNO_B:SNO_T ratios are 1.2 in the Northern Hemisphere and 1.1 in the Southern Hemisphere, indicating a slightly greater biological contribution to SNO. Computing SNO_B and SNO_T values between 30° and 60° latitude yielded SNO_B:SNO_T ratios of 1.3 and 1.2 in the Northern and Southern Hemispheres, suggesting a somewhat greater biological than thermal contribution to SNO in the temperate regions. In general, different latitudinal bands have distinct biological and thermal contributions to SNO. The global pattern of SNO is similar in each major basin. The Atlantic, Pacific, and Indian Basins have SNO_B:SNO_T ratios in each hemisphere ranging between 0.9 and 1.1. The Southern Hemisphere's SNO_B and SNO_T values are greater than in the North-

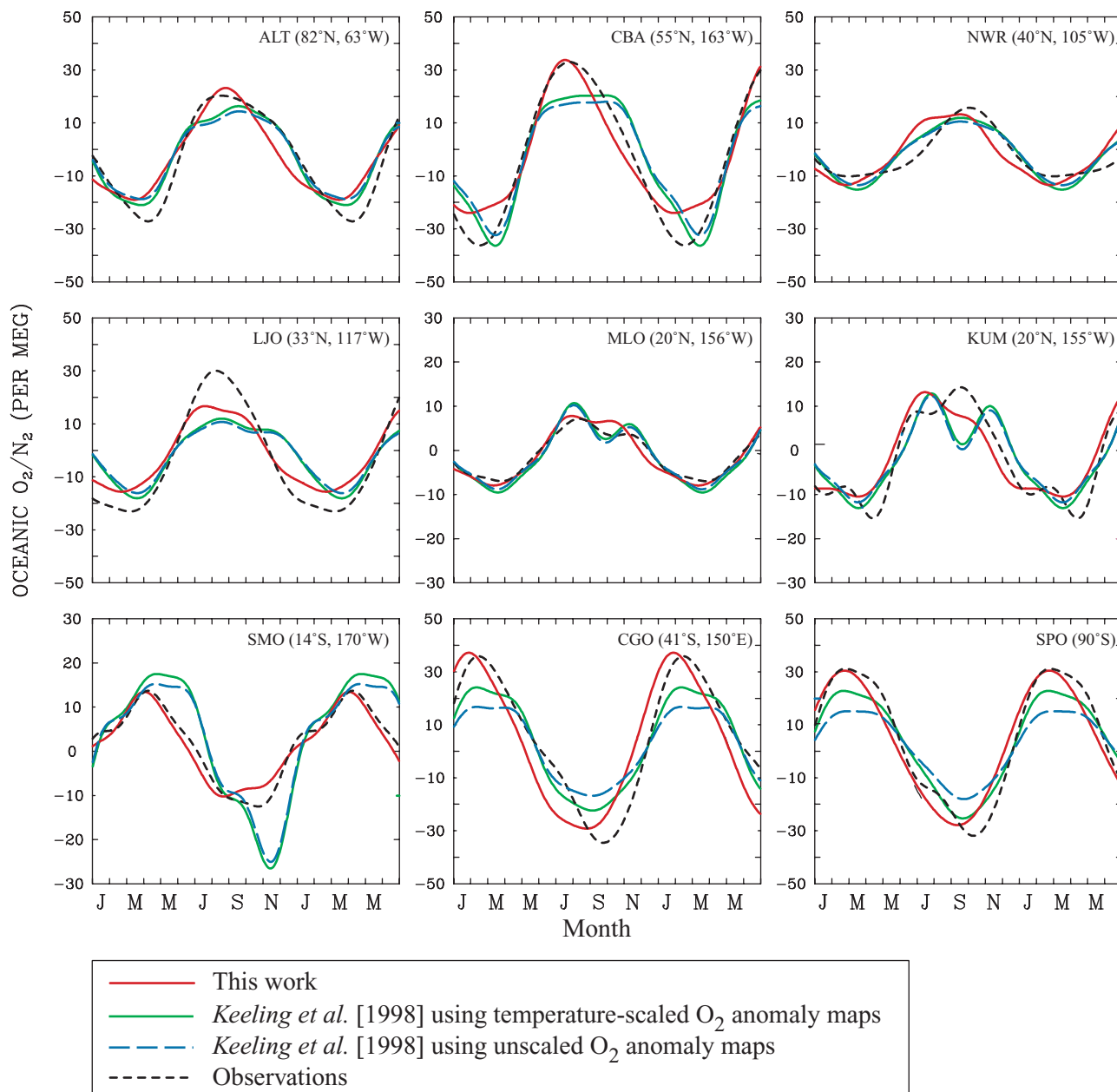


Plate 4c. Comparison between the model-simulated and observed oceanic component of the air O₂/N₂ variations at the Pacific Ocean baseline stations for the present O₂ flux climatology (red solid line) and the Keeling et al. [1998] flux data using both unscaled (blue stippled line) and SST-scaled O₂ anomaly data (green solid line) on the basis of the Najjar and Keeling [1997] climatology. The simulated curves include the N₂ component based on net heat flux data (same as the solid line labeled N in Plate 4a). The dashed curve represents the observed oceanic component of the O₂/N₂ cycle based on least squares fit to the observations using a terrestrial O₂:C ratio of 1.1 (same as dashed black line in Plate 4a).

ern Hemisphere by about 1.7 and 1.8. The difference can be explained in part because of the greater mean ice-free ocean area of the Southern Hemisphere compared to the mean ice-free ocean area of the Northern Hemisphere (about 1.4 larger). Our calculated thermal and biological SNO values for the extratropical regions ($\geq 30^\circ$ latitude) account for about 77% of the SNO₇ and 92% of the SNO_B hemispheric results. Our estimate essentially omits equatorial and other oceanic areas where the seasonal O₂ flux variation is not well resolved.

We summed the Northern and Southern Hemispheric SNO values to estimate a global SNO of about 8.6 (Table 6). The

Northern and Southern Hemispheres contribute 36 and 64% of the global SNO. On basin scales the Pacific is the largest contributor (50%) to the global SNO, followed by the Atlantic (30%) and the Indian Basins (20%). The basin-wide SNO value depends on the choice of geographical boundaries of each basin and non-ice-covered oceanic regions. To gain insight into how representative our simulated oxygen fluxes are without atmospheric calibrations, we compared the calculated hemispheric SNO values against SNO values estimated using the calibration coefficients listed in Table 4. We multiplied the fluxes poleward of 30° latitude by 1.09 in the Northern Hemisphere and by 0.97

Table 4. Comparison of Scaling Factors for Optimal Fits Between *Keeling et al.* [1998] for the Data of *Najjar and Keeling* [1997] and This Work^a

Station Code	<i>Keeling et al.</i> [1998]	This Work
ALT	1.16 ± 0.09	1.07 ± 0.15
CBA	1.11 ± 0.12	1.16 ± 0.10
NWR	0.94 ± 0.11	0.89 ± 0.18
LJO	1.59 ± 0.25	1.52 ± 0.08
KUM	1.05 ± 0.19	1.07 ± 0.16
MLO	0.81 ± 0.05	0.84 ± 0.06
SMO	0.61 ± 0.10	1.07 ± 0.09
CGO	1.24 ± 0.10	0.91 ± 0.16
SPO	1.22 ± 0.54	1.01 ± 0.11
ALT, NWR, CBA	1.15 ± 0.05	1.09 ± 0.09
CGO, SPO	1.23 ± 0.06	0.97 ± 0.08
All stations	1.14 ± 0.05	1.01 ± 0.07

^aThe uncertainties (± standard error) on the scaling factors represent the standard errors to the fits.

in the Southern Hemisphere. The choice of calibration factors is to some extent arbitrary because the optimized fluxes are sensitive to the atmospheric observations in the Pacific stations. Nevertheless, we used these calibration factors because most of the oceanic contribution to the atmospheric O₂/N₂ variations at the Pacific baseline stations appears to be caused by seasonal air-sea variations poleward of 30° latitude [*Keeling et al.*, 1998]. We found that the difference between the uncalibrated (8.6) and calibrated (8.7) sum of hemispheric SNO values is small, about 1%. The small difference is not surprising because the high-latitude calibration values and the averaged calibration factors for all the baseline stations combined is about 1 (Table 4).

We also calculated SNO values from the *Najjar and Keeling* [2000] climatology as shown in Table 6. Hemispheric SNO estimates calculated using the two climatologies are similar (about 3% smaller in the Northern Hemisphere and 3% larger in the Southern Hemisphere). However, we found that the distribution of SNO values with latitude is different. Whereas the *Najjar and Keeling* [2000] climatology yields 85% (Northern Hemisphere) and 72% (Southern Hemisphere) of the hemispheric SNO in the extratropics, our climatology yields 82% (Northern Hemisphere) and 86% (Southern Hemisphere) of hemispheric SNO in the extratropics. Particularly in the Southern Hemisphere, our climatology has larger seasonal fluxes at higher latitudes and lower fluxes at lower latitudes than the *Najjar and Keeling* [2000] climatology. The present O₂ flux climatology is probably more realistic on the basis of the comparison with the atmospheric observations at Samoa (14°S), Cape Grim (41°S), and the South Pole (90°S) (Plate 4c).

11. Carbon Production Estimates

Following *Keeling and Shertz* [1992], *Najjar and Keeling* [2000] used the biological SNO values computed from their

O₂ flux climatology to estimate extratropical (>20° latitude) biological new production in the mixed layer during the shoaling period. First, they calculated SNO_B for each 10° latitudinal band poleward of 20°N and 20°S and excluded from their calculations the north Indian Ocean. They then added up the SNO_B values for individual 10° latitudinal bands and reported a spring-summer mixed layer new production of 4.5 (without atmospheric calibrations) and 5.6 Pg C (with atmospheric calibrations) assuming an O₂:C ratio of 1.45 (1 Pg = 10¹⁵ g). If we add up individual 10° latitude bands poleward of 20° (excluding the north Indian Ocean following *Najjar and Keeling* [2000]), we calculated a global SNO_B value equivalent to 3.7 Pg C on the basis of the present O₂ flux climatology and an O₂:C ratio of 1.45. Our global SNO_B estimate is insensitive to atmospheric calibrations within 2%, whereas the *Najjar and Keeling* [2000] global SNO_B estimate increases significantly with the atmospheric calibrations by about 20%. Our carbon production estimates are smaller than those of *Najjar and Keeling* [2000]. The discrepancies between the estimates include differences between the O₂ anomaly climatologies, the calculation of thermal fluxes, and the choice of geographic boundaries of the oceanic basins and non-ice-covered oceanic regions.

Following *Najjar and Keeling* [2000], we can compare our estimates of carbon production based on SNO_B with satellite estimates of carbon primary production. *Najjar and Keeling* [2000] computed an extratropical seasonal primary production of 11.8 Pg C in the mixed layer on the basis of the primary production data of *Antoine et al.* [1996] based on Coastal Zone Color Scanner (CZCS) chlorophyll observations and computed an *f* ratio (the ratio of new to total primary production) of 0.38–0.46. Using their 11.8 Pg C estimate of seasonal primary production and our estimate of carbon production of 3.7 Pg C, we derive an *f* ratio of ~0.3. Caution must be exercised in interpreting SNO_B values strictly in relation to carbon new production. The assumption that the seasonal O₂ outgassing approximates net community O₂ production during the seasonal period of shoaling mixed layer has been shown to yield reasonable results locally [*Jenkins and Goldman*, 1985; *Emerson*, 1987], although it is only approximately correct. Oxygen outgassing could be smaller than carbon production to the extent that some of the seasonal O₂ production is stored in the mixed layer, or it could be either larger or smaller than carbon production to the extent that the air-sea O₂ flux is also influenced by exchanges of O₂ with deeper waters.

12. Summary and Conclusions

Here we present an improved global monthly climatology of surface O₂ anomalies and air-sea fluxes based on a weighted linear least squares approach. The regressions use seasonal heat flux anomalies for spatial and temporal interpolation of historical O₂ data. The method gives a robust relation for estimating the large-scale mean seasonal distribution of O₂ anomalies and fluxes. We concentrate primarily on the distribution of the global air-sea seasonal O₂ flux.

Table 5. Thermal (SNO_T) and Biological (SNO_B) Values (10¹⁴ mol O₂) Based on the Weighted Global Regression Coefficients for the Ice-Free Surface Global Ocean (Global), Atlantic (ATL), Pacific (PAC), and Indian (IND) Basins

Latitudinal Band	Global SNO _T	Global SNO _B	ATL SNO _T	ATL SNO _B	PAC SNO _T	PAC SNO _B	IND SNO _T	IND SNO _B
0°–80°N	1.59	1.53	0.71	0.55	0.91	0.86	0.027	0.04
0°–80°S	2.87	2.62	0.62	0.66	1.28	1.33	0.77	0.84
30°–80°N	1.18	1.39	0.65	0.42	0.81	0.61	0	0
30°–80°S	2.25	2.44	0.58	0.54	1.20	1.02	0.70	0.65
60°–80°N	0.18	0.09	0.09	0.08	0.01	0.02	0	0
60°–80°S	0.36	0.10	0.01	0.06	0.03	0.19	0.02	0.07

Table 6. Total (SNO) and Biological (SNO_B) Seasonal Net Outgassing ($\times 10^{14}$ mol O₂) Based on the Weighted Global Regression Coefficients for the Ice-Free Surface Oceanic Domain^a

Latitudinal Band	This Work SNO	This Work SNO _B	NK00 SNO	NK00 SNO _B
0°–80°N	3.12	1.53	3.22	1.90
0°–80°S	5.49	2.62	5.34	3.23
30°–80°N	2.57	1.39	2.72	...
30°–80°S	4.69	2.44	3.84	...
60°–80°N	0.26	0.09
60°–80°S	0.27	0.10

^a We list the SNO values that we calculated using the *Najjar and Keeling* [2000] (NK00) climatology. The SNO_B values of NK00 correspond to their reported values. In all cases, SNO and SNO_B are computed using O₂ fluxes without atmospheric calibrations.

Model-simulated seasonal oceanic air-sea O₂/N₂ contributions to the atmosphere compare well with seasonal variations in atmospheric O₂/N₂ ratios at baseline stations in the Pacific Ocean. Optimization of the gas-exchange velocity for O₂ by means of scaling factors shows that little adjustment is necessary between the simulated and observed O₂/N₂ variations. This substantiates that the present O₂ anomaly climatology together with the wind exchange velocity formulation of *Wanninkhof* [1992] for steady wind conditions provides a robust measure of the air-sea O₂ flux. Our study suggests that the component of the air-sea O₂ flux that correlates with heat flux dominates the large-scale air-sea O₂ exchange on seasonal timescales. The results are useful as constraints on global seasonally resolved models.

The global seasonal net oxygen outgassing is estimated to be about 0.9 Pmol O₂ (1 Pmol = 10¹⁵ mol). Evaluation of the seasonal air-sea O₂ flux attributable to thermal and biological sources indicates that the two components make roughly equal contributions to the seasonal air-sea exchange on hemispheric scales. The seasonal net thermal and biological outgassing contributions to the total varies within latitudinal bands. The extratropical (>20°) biological seasonal net outgassing is equivalent to a seasonal carbon production of about 3.7 Pg C based on an O₂:C ratio of 1.45.

Acknowledgments. This work was completed while H. G. was a postdoctoral researcher at Scripps Institution of Oceanography. Use of the UCSD Cray computer facilities is acknowledged. Steve Piper provided initial guidance on the use of the TM2 model. This work benefited from helpful comments and data provided by Ray Najjar. Comments by Andrew Dickson and two anonymous reviewers were helpful. This work was supported by a NASA grant (NAG5-6668). This is U.S. JGOFS contribution 718.

References

- Antoine, D., J. M. Andre, and A. Morel, Oceanic primary production, 2, Estimation at global scale from satellite (Coastal Zone Color Scanner) chlorophyll, *Global Biogeochem. Cycles*, 10, 57–70, 1996.
- Benson, B. B., and O. Krause, The concentration and isotopic fractionation of oxygen dissolved in freshwater and seawater in equilibrium with the atmosphere, *Limnol. Oceanogr.*, 10, 264–277, 1984.
- Emerson, S., Seasonal oxygen cycles and biological new production in surface waters of the subarctic Pacific Ocean, *J. Geophys. Res.*, 92, 6335–6544, 1987.
- Garcia, H., On the large-scale characteristics, fluxes, and variability of the North Atlantic Deep Water and its Deep Western Boundary Current deduced from nutrient and oxygen data, Ph.D. thesis, 184 pp., Oregon State Univ., Corvallis, 1996.
- Garcia, H., and L. Gordon, Oxygen solubility in seawater: Better fitting equations, *Limnol. Oceanogr.*, 37, 1307–1312, 1992.
- Garcia, H., A. Cruzado, L. Gordon, and J. Escanez, Decadal-scale chemical variability in the subtropical North Atlantic deduced from nutrient and oxygen data, *J. Geophys. Res.*, 103, 2817–2830, 1998.
- Gibson, J. K., P. Kallberg, S. Uppala, A. Hernandez, A. Nomura, and E. Serrano, ERA description, *ECMWF Re-Anal. Proj. Rep. Ser. 1*, 72 pp., Eur. Cent. for Medium-Range Weather Forecasts, Reading, England, U.K., 1997.

- Hasse, L., The sea-surface temperature deviation and heat flow at the air-sea interface, *Boundary Layer Meteorol.*, 1, 368–379, 1971.
- Heiman, M., The global atmospheric tracer model TM2, *Tech. Rep. 9*, pp. 1–51, Dtsch. Klimarechenzentrum, Hamburg, Germany, 1995.
- Heiman, M., and C. D. Keeling, A three-dimensional model of atmospheric CO₂ transport based on observed winds, 2, Model description and simulated tracer experiments, in *Aspects of Climate Variability in the Pacific and Western Americas*, *Geophys. Monogr. Ser.*, vol. 55, edited by D. H. Peterson, pp. 237–275, AGU, Washington, D. C., 1989.
- Jenkins, W. J., and W. B. Goldman, Seasonal oxygen cycling and primary production in the Sargasso Sea, *J. Mar. Res.*, 43, 465–491, 1985.
- Keeling, R. F., and S. R. Shertz, Seasonal and interannual variations in atmospheric oxygen and implications for the carbon cycle, *Nature*, 358, 723–727, 1992.
- Keeling, R., R. Najjar, M. Bender, and P. Tans, What atmospheric oxygen measurements can tell us about the global carbon cycle, *Global Biogeochem. Cycles*, 7, 37–67, 1993.
- Keeling, F. R., B. B. Stephens, R. G. Najjar, S. C. Doney, D. Archer, and M. Heimann, Seasonal variations in the atmospheric O₂/N₂ ratio in relation to the kinetics of air-sea exchange, *Global Biogeochem. Cycles*, 12, 141–163, 1998.
- Millero, F. S., and A. Poisson, International one-atmosphere equation of state of seawater, *Deep Sea Res., Part A*, 34, 1981–2003, 1981.
- Najjar, R., and R. Keeling, Analysis of the mean annual cycle of the dissolved oxygen anomaly in the world ocean, *J. Mar. Res.*, 55, 117–151, 1997.
- Najjar, R., and R. Keeling, Mean annual cycle of the air-sea oxygen flux: A global view, *Global Biogeochem. Cycles*, 14, 573–584, 2000.
- Oberhuber, J. M., An atlas based on the COADS set: The budgets of heat, buoyancy and turbulent kinetic energy at the surface of the global ocean, *Rep. 15*, pp. 1–20, Max-Planck-Inst. für Meteorol., Hamburg, Germany, 1988.
- Reid, J. L., On the total geostrophic circulation of the South Atlantic: Flow patterns, tracers, and transports, *Prog. Oceanogr.*, 23, 149–244, 1989.
- Reid, J. L., On the total geostrophic circulation of the North Atlantic: Flow patterns, tracers, and transports, *Prog. Oceanogr.*, 33, 1–92, 1994.
- Saunders, P. M., The accuracy of measurements of salinity, oxygen and temperature in the deep ocean, *J. Phys. Oceanogr.*, 16, 189–195, 1986.
- Schudlich, R., and S. Emerson, Gas supersaturation in the surface ocean: The roles of heat flux, gas exchange, and bubbles, *Deep Sea Res., Part II*, 43, 569–589, 1996.
- Shea, D. J., K. E. Trenberth, and R. W. Reynolds, A global monthly sea surface temperature climatology *J. Clim.*, 5, 987–1001, 1992.
- Wanninkhof, R., Relation between wind speed and gas exchange over the ocean, *J. Geophys. Res.*, 97, 7337–7382, 1992.
- Weiss, R.F., Solubility of nitrogen, oxygen, and argon in water and seawater, *Deep Sea Res. Oceanogr. Abstr.*, 17, 721–735, 1970.
- Wright, P., An atlas based on the “COADS” set: Fields of mean wind, cloudiness and humidity at the surface of the global ocean, *Rep. 14*, 22 pp., Max-Planck-Inst. für Meteorol., Hamburg, Germany, 1988.

H. E. Garcia, Ocean Climate Laboratory, NOAA/NODC, 1315 East-West Highway, Silver Spring, MD 20910-3282, USA. (Hernan.Garcia@noaa.gov)

R. F. Keeling, Scripps Institution of Oceanography, University of California, 9500 Gilman Drive, San Diego, La Jolla, CA 92093-0244, USA.

(Received December 28, 1999; revised July 17, 2001; accepted July 23, 2001.)